Quantum well states and oscillatory magnetic interlayer coupling

2002 J. Phys.: Condens. Matter 14 R169

(http://iopscience.iop.org/0953-8984/14/8/201)

INSTITUTE OF PHYSICS PUBLISHING JOURNAL OF PHYSICS: CONDENSED MATTER

J. Phys.: Condens. Matter **14** (2002) R169–R193 PII: S0953-8984(02)29939-7

TOPICAL REVIEW

Quantum well states and oscillatory magnetic interlayer coupling

Z Q Qiu[1,2] **and N V Smith**[3]

[1] Department of Physics, University of California at Berkeley, USA
[2] Materials Science Division, Lawrence Berkeley National Laboratory, Berkeley, CA 94720, USA
[3] Advanced Light Source, Lawrence Berkeley National Laboratory, Berkeley, CA 94720, USA

Received 24 October 2001
Published 15 February 2002
Online at stacks.iop.org/JPhysCM/14/R169

Abstract

Some interesting magnetic properties of artificially layered metallic materials are strongly connected with the existence of electron standing waves, or quantum well (QW) states. One such property is the oscillation in exchange coupling between two ferromagnetic materials separated by a nonmagnetic spacer layer of varying thicknesses. This article summarizes the findings of an extended investigation of QW states and their relation to oscillatory magnetic interlayer coupling carried out using angle-resolved photoemission with synchrotron radiation and auxiliary techniques such as magnetic x-ray linear dichroism and surface magnetic optical Kerr effect. A key feature of the measurements was the use of wedge-shaped samples, which, in combination with the small spot size of the synchrotron source, permitted investigation of the entire layer thickness range in a single experiment. Single-wedge samples were used as well as double-wedge samples tapered in orthogonal directions. The systematics of QW formation are well understood in terms of the elementary quantum mechanics of a particle in a box. We treat a single well, a double well and a corrugated well. The work on single wells focused on the elucidation of the long and short magnetic oscillatory periods for a Cu spacer layer, and their relation to the belly and neck regions of the Cu Fermi surface. The effects of interfacial roughness and interfacial mixing were investigated. The studies on double wells focused on the controllable degree of tunnelling between the wells and the avoided crossings that occur when the QW energies in one well are swept through those of the other. Finally, we consider the QW wavefunctions and their envelope modulation. The latter can be understood in terms of Bragg diffraction within a corrugated well. With use of a double-wedge-shaped sample it has proved possible to pass a thin probe across the well and to detect experimentally the envelope modulation.

(Some figures in this article are in colour only in the electronic version)

1. Introduction

1.1. Motivation

Magnetism is a consequence of electron spin alignment and the removal of spin degeneracy by exchange interaction. Artificially produced magnetic layered structures with thicknesses on the nanometre scale display interesting new properties not seen in the bulk. This has opened up the area of *spintronics*, the development of devices whose operation derives from electron spin dynamics rather than charge dynamics. Over the last two decades there have been steady advances in synthesis techniques and theoretical understanding holding out the prospect of rational engineering of magnetic nanostructures with desirable properties. In this article we highlight just one aspect of these developments: the existence of quantum well (QW) states and their relation to *oscillatory* magnetic interlayer coupling as revealed by photoemission spectroscopy using synchrotron radiation.

1.2. Historical background

Antiferromagnetic coupling (AFC) between two magnetic layers across a nonmagnetic intervening layer was first discovered in an Fe/Cr sandwich in 1986 [1]. The interlayer coupling across the Cr layer results in an opposite pointing direction of the two Fe layer magnetizations. Two years later, giant magneto-resistance (GMR) was observed in an antiferromagnetically coupled Fe/Cr superlattice with a resistivity drop of an order of magnitude after aligning all Fe layer magnetizations with an external magnetic field [2]. These discoveries stimulated a great deal of activity within the materials physics community due to the high potential for application in the magnetic recording industry. Thanks to the rapid technology, devices based on the GMR phenomenon are already being incorporated in today's computer read heads for high-density recording. The magnetic coupling in the Fe/Cr superlattice was later found to oscillate between AFC and ferromagnetic coupling (FC) as the Cr spacer layer thickness was increased. Many other systems, such as Fe/Cu [3], Fe/Mo [4], Co/Ru [5] and Co/Ru [6], were also found to behave similarly to Fe/Cr. All of these systems exhibit oscillations between AFC and FC with an oscillation periodicity of the spacer layer thickness of $\sim$10 Å. The oscillatory behaviour led to the proposal of Rudermann–Kittel–Kasuya–Yosida (RKKY) interaction as the origin of the magnetic coupling; i.e., spin-dependent scattering of electrons at the magnetic/nonmagnetic interface mediates the interlayer coupling across the spacer layer. The RKKY theory shows an oscillation periodicity of $\pi/|\boldsymbol{k}_{BZ} - \boldsymbol{k}_F|$ [7] at the saddle points of the Fermi surface, which not only explained the existing of long-period oscillations but also predicted the existence of 1–3 monolayer (ML) short-period oscillations. The absence of short-period oscillations in earlier experiments is probably due to a greater interfacial roughness than the short periodicity. With an advanced molecular beam epitaxy (MBE) technique, short-period ($\sim$2 ML) oscillations of the interlayer coupling were first observed in the Fe/Cr system [8, 9], and later in Fe/Mn [10], Fe/Au [11], Fe/Mo [12], Co/Cu [13] and Fe/Ag [14] systems. The experimental observations of the oscillation periodicity agree very well with the RKKY theory.

Parallel to the RKKY theory, QW states were also brought to the agenda. As the size of a physical system is reduced to the nanometre range, electron confinement is expected to generate QW states. Thus if QW states are a general character of magnetic nanostructures, it is natural to speculate on their connection with the newly discovered phenomena. In fact QW theories were also proposed to explain the magnetic interlayer coupling [15–17]. Noting that RKKY and QW theories give the same oscillation periodicity, experimental effort in searching for the origin of the interlayer coupling was then devoted to the dependence of the interlayer coupling on the *ferromagnetic* layer thickness. Qiu *et al* performed an experiment on Co/Cu(wedge)/Co

sandwiches with 8, 14 and 20 ML Co, and found that the AFC peak positions are independent of the Co layer and that the saturation magnetic field is roughly inversely proportional to the Co layer thickness [18], thus supporting the interfacial effect of the magnetic coupling. However, more detailed work on the Co/Ni/Co/Cu/Co/Ni/Co system [19], the Fe/Cr system [20] and the Fe/Au [21] system revealed that the coupling strength actually depends on the magnetic layer thickness. Moreover, the coupling was recently found even to oscillate with the thickness of a cap Cu layer on top of a Co/Cu/Co sandwich [22]. All these results imply that each layer in an entire multilayer stack is relevant to the magnetic coupling, suggesting that the coupling is not a sheer interfacial effect. The latter discoveries gave a strong indication of the QW nature of the magnetic interlayer coupling [23,24]. The interesting questions are then (1) do the QW states exist in magnetic nanostructures? (2) how do the QW states behave in metallic systems? and (3) what is the relation between the QW states and the magnetic interlayer coupling?

QW states in metallic thin films were first discovered in the nonmagnetic Ag/Au(111) system [25] where the band gap of Au confines Ag electrons. QW states in magnetic multilayers were first observed in the Cu/Co/Cu(100) system where the density-of-states (DOS) at the Fermi level (E_F) of Cu film was found to oscillate with the same long-period oscillations in the magnetic interlayer coupling [26]. Because of the spin-dependent energy band in magnetic metals, the QW states in the nonmagnetic spacer layer are found to be spin dependent [27]. With the QW picture, the dependence of the interlayer coupling on the ferromagnetic layer thickness can then be understood as a result of a quantum interference effect [28]. Despite this qualitative progress in the coupling study, several important issues remained unclear. One of the basic open questions is the relation between long-period (∼10–18 Å) and short-period (∼3–6 Å) oscillations. Magnetic measurements suggest that the long- and short-period couplings are correlated with a relative phase and amplitude [29].

To better understand the physical origin of the interlayer coupling, several groups recently performed angle-resolved photoemission spectroscopy (ARPES) experiments to investigate the QW states, aiming to identify the roles of Fermi electrons at different locations in momentum space. For example, Segovia *et al* [30] studied the Cu/Co(100) system at the neck of the Cu dog bone Fermi surface and identified the existence of a new set of QW states in addition to the QW states at the belly of Fermi surface. But it is not conclusive on whether or not there exists short-period oscillation at the Fermi level. The short-period oscillations in the DOS at the neck of the Fermi level (E_F) were only recently observed by Kläsges *et al* [31]. Curti *et al* [32] performed inverse photoemission for 2, 3 and 4 ML Cu on Co(100) near the neck of the Fermi surface and focused on the dispersion of the QW energy with the in-plane momentum, but did not explore the relation between the long- and short-period oscillations. Li *et al* [33] studied the QW states in the Cr/Fe(100) system and singled out the origin of the long-period oscillations, but were inconclusive on the short-period DOS oscillations at E_F.

1.3. Scope and structure of this article

The above account indicates that a comprehensive study on the QW states and their relation to the interlayer magnetic coupling is needed in order to provide a clearer physical picture on the coupling mechanism. With this motivation, we and our colleagues have carried out an investigation over the last a few years on QW states using ARPES at the advanced light source (ALS) of the Lawrence Berkeley National Laboratory. The intent of this article is to summarize our findings.

The systematics of our experimental results can be understood qualitatively and even quantitatively using the elementary quantum mechanics of a particle in a box. Indeed this serves as a unifying thread that runs through the article. The progression of the article and the

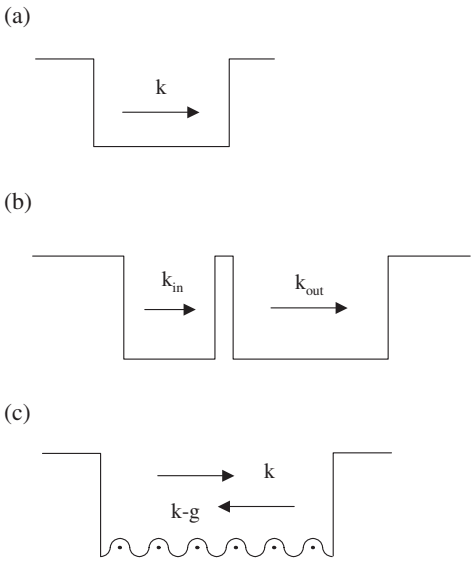

Figure 1. Particle in a box. The three kinds of box used in the discussion of QW states: (a) a single flat box supporting plane waves with wavevectors k; (b) a double potential well with waves k_{in} and k_{out} that can be coupled across the barrier; (c) a corrugated box in which the plane wave k is back-diffracted into plane wave $k–g$.

various boxes that we shall deal with are illustrated in figure 1. In section 3, we present results understandable in terms of electrons in a single flat box (figure 1(a)). In section 4, we deal with double wells separated by a controllable tunnelling barrier (figure 1(b)). Finally, in section 5, we turn from an account of merely the energetics of the QW states to the consideration of the QW wavefunctions. It has proved possible to detect the envelope modulation of the QW wavefunction, and the essential physics is readily understood in terms of a particle in a corrugated box (figure 1(c)).

2. Experimental approach

2.1. Wedge-shaped samples

The experimental system we have concentrated on is Cu on Co/Cu(100). We chose this system for the following reasons. First, Cu/Co(001) has become a representative system for QW studies in magnetic nanostructures. Second, Cu has a simple Fermi surface whose sp band can be easily separated from other energy bands. Finally, Cu and Co films grow epitaxially on each other in the (100) orientation, giving rise to an atomically flat interface.

A 10 mm diameter Cu(001) single crystal was first mechanically polished down to 0.25 μm diamond-paste, followed by electropolishing. The substrate was then introduced into an ultrahigh vacuum system and cleaned by cycles of Ar^+ sputtering at $\sim$2 keV and annealing at 600–700 °C. All samples were grown at room temperature by evaporating Co, Cu and Ni from alumina crucibles heated with tungsten wires. Typical evaporation rates were about 1 ML min^{-1} for Co and Ni, and 3 ML min^{-1} for Cu. The pressure during sample growth remains below 1×10^{-9} Torr. A knife-edge shutter was placed $\sim$1 mm in front of the substrate. Wedge-shaped samples were made by translating the substrate behind the shutter during the film growth. The slope of the wedge is controlled by the moving speed of the substrate.

Wedge-shaped samples were crucial for this study. With a single sample it is possible to investigate the entire thickness range. The effects we were looking for were often subtle and would have been obscured by fluctuations in preparation conditions if we had had to prepare a separate sample for each thickness. Our apparatus also permits the preparation of *double-wedge* samples in which it is possible to deposit two layers which are tapered in orthogonal directions. This capability has been used in the investigation of tunnelling between double quantum wells. It has also been used to move a probing 'finger' across a single well.

2.2. Photoemission with synchrotron radiation

Photoemission spectroscopy currently provides the most direct observation of the QW states below the Fermi level. Since photoemission intensity is roughly proportional to the DOS of the occupied levels, the formation of QW states at discrete energy levels manifests itself as peaks in the photoemission energy spectrum. To have a quantitative study of QW states at atomic scale, a careful thickness-dependent photoemission measurement with high signal-to-noise ratio is demanded. To take advantage of the wedge-shaped samples, it is essential to have a well focused spot of light so that variation in sample thickness is negligible across the diameter of the spot. The high brightness of the ALS, a third-generation synchrotron light source, delivers such a small spot. Beamline 7.0 at the ALS can reduce the photon beam size down to 50–100 μm with a high enough photon flux ($>10^{12}$ photons per second at resolving power of 10 000) to make local photoemission measurements. Thus for a wedge of $\sim$5–10 ML mm^{-1} slope, a scan of a 50 μm photon beam across the sample will provide a systematic thickness-dependent measurement with $\sim$0.25–0.5 ML thickness resolution.

Another advantage of synchrotron radiation is its wide spectrum and the possibility of elemental analysis using core-level photoemission. We have monitored the Cu and Co 3p core-level photoemission to calibrate the starting position of the wedges. Access to the core levels enables the auxiliary technique of magnetic x-ray linear dichroism (MXLD), that can be used to determine the direction of magnetization of a layer.

The photoemission measurements were performed using a hemispherical analyser. The total resolution (electron + photon) was better than 60 meV. The total angular acceptance was about 1.5°. Under these conditions, the photoemission energy spectrum essentially measures the local DOS of the sample near the surface (within the escape depth of the photoelectrons). Since the in-plane momentum of electrons is conserved as an electron leaves the sample surface, ARPES determines the electronic structure in momentum space by detecting photoelectrons at an angle relative to the surface normal.

For the case of Cu(001), we shall focus on the belly and neck of the Fermi surface where the electron group velocity is perpendicular to the film surface, as illustrated in figure 2. For electronic states at the belly of the Cu Fermi surface, 83 eV photon energy was used and normal emission measurements were taken. For electronic states at the neck of the Cu Fermi surface, 77 eV photon energy was used and photoemission measurements were made at 11° off the surface normal direction in the (011) plane. Energy spectra were taken at various Cu thicknesses to construct the QW image. Once the experimental conditions are correctly set, the whole measurement takes only $\sim$30 min.

2.3. Auxiliary techniques

Magnetic interlayer coupling can be determined by MXLD and surface magneto-optic Kerr effect (SMOKE) techniques. For MXLD measurement, normal photoemission from the Co 3p level was measured [34]. The incident 130 eV photon beam was p polarized

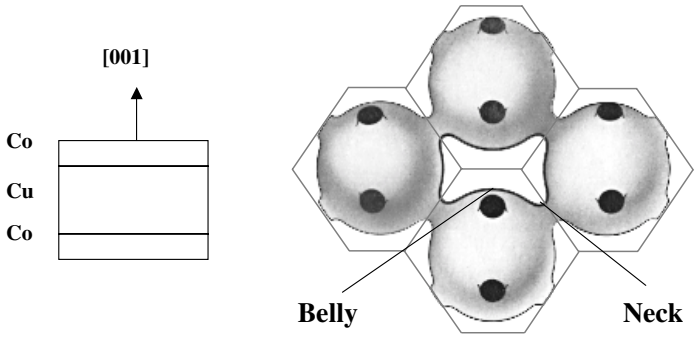

Figure 2. Schematic drawing of the Co/Cu/Co(001) sandwich and the Cu Fermi surface showing the belly and neck regions.

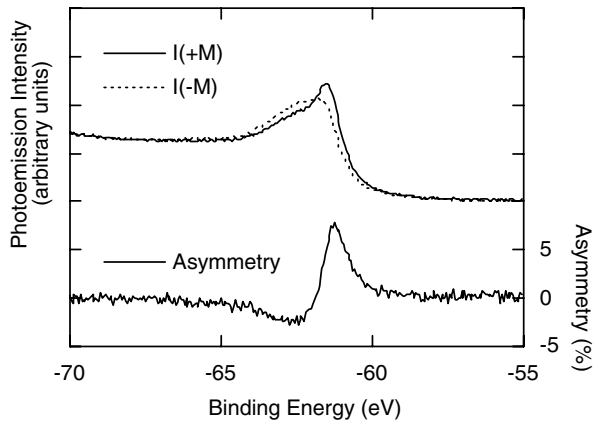

Figure 3. MXLD showing the difference in photoemission from the 3p level of 15 ML Co grown on Cu(001) obtained with linearly polarized off-normal incident x-rays for the two directions of magnetization M.

(in the plane of incidence) with an incident angle of $\theta = 30^\circ$ (measured from the sample surface). Figure 3 shows the 3p core-level spectra from a 15 ML Co film grown on Cu(100). The $+M$ and $-M$ are the two opposite magnetization directions which are in the film plane but perpendicular to the photon incident plane. This geometry is similar to the transverse SMOKE measurement. Because of the spin–orbit interaction, different magnetization directions have different photoemission intensity. The MXLD asymmetry, defined as $[I(+M) - I(-M)]/[I(+M) + I(-M)]$, thus measures the presence of magnetic order and is sensitive to the magnetization direction. To measure the interlayer magnetic coupling between the Co layers across the Cu spacer, the sample was magnetized with a pulsed magnetic field prior to the MXLD measurement. Because of the surface sensitivity of MXLD, the magnetization direction of the top Co layer determined from MXLD thus determines the sign of the magnetic interlayer coupling.

To obtain the coupling strength, magnetic hysteresis loops of the films were measured using the SMOKE technique. An intensity-stabilized, He–Ne laser was used as the light source. A linear polarizer polarized the incident light in the plane of incidence (p-polarization). The angle of the incidence light is 45° from the surface normal. Upon reflection from the sample surface the light passes through an analysing polarizer set at $\delta \sim 1^\circ$ from extinction, and a

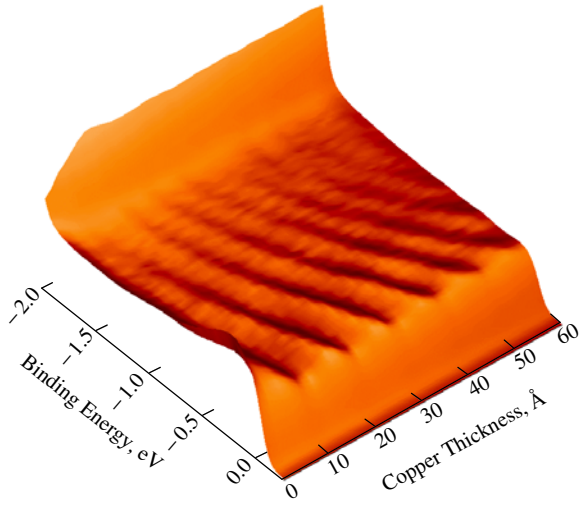

Figure 4. Photoemission spectra taken along the surface normal corresponding to the belly direction of the Cu Fermi surface as indicated in figure 2. Oscillations in intensity as a function of the Cu thickness and electron energy show the formation of QW states in the Cu layer.

quarter-wave plate is used to remove the birefringence of the UHV window. The light intensity, referred to as the Kerr intensity, is then detected by a photodiode and recorded as a function of the applied magnetic field to generate the hysteresis loop. For the experimental system in this paper, the magnetization is in the film plane so that only longitudinal SMOKE measurements were performed.

3. Single quantum wells

We first studied QW states in a single Cu layer. The purpose of this study is to understand the behaviour of single QW states quantitatively. About 36 Å (∼20 ML) of fcc Co(100) was grown on a Cu(100) single crystal to serve as the Co substrate. A Cu wedge was then grown on top of the Co layer. Figure 4 shows the photoemission intensity at the belly of the Fermi surface as a function of Cu film thickness and electron energy. The rise of the intensity at 2.0 eV below the Fermi level is due to the Cu 3d energy band. Since bulk Cu has a featureless sp band between 0.0 and −2.0 eV, the oscillations in the photoemission intensity as a function of energy for fixed Cu thickness and as a function of Cu thickness for fixed energy clearly show the existence of the QW states of the sp electrons in the Cu layer. The suppression of the substrate Co 3d peak (at binding energy ∼0.0 eV) above ∼10 Å Cu thickness indicates that the escaping distance of the photoelectrons is less than 10 Å. It is worth emphasizing that the measurement was made at room temperature, thus the result of figure 4 demonstrates the existence of QW states at room temperature. This is the advantage of metallic nanostructures, that the quantized energy splitting is greater than the room temperature thermal energy although it is an experimental challenge to control nanometre size precisely. This property is very important to technology development because the ideal device working temperature is room temperature. It is worthwhile to point out two special features in figure 3. First, the oscillation periodicity (5.88 ML) at the Fermi level is not π/k_F but $\pi/|\boldsymbol{k}_{BZ} - \boldsymbol{k}_F|$ which is exactly the periodicity of the long-period magnetic interlayer coupling in the Co/Cu/Co(001) system. Second, the QW state energy increases with Cu film thickness. As will be shown in the next section, these two characters are from the same origin.

3.1. Particle in a flat box

To gain a quantitative understanding, we calculated QW state positions in the energy–thickness plane using the so-called phase accumulation model (PAM) where electrons inside Cu are confined in a potential well of width d_{Cu} [35]. This is nothing more than the elementary quantum mechanics of a particle in a flat box of the kind depicted in figure 1(a). The quantization condition for an electron state in such a potential box is given by

$$2kd_{\mathrm{Cu}} + \phi_C + \phi_B = 2\pi n \qquad n = \text{integer} \tag{1}$$

where ϕ_B and ϕ_C are the phase gains of the electron wavefunction upon reflection at the two boundaries of the box, n is the number of half-wavelengths confined inside the QW and k describes the Cu electron wavevector component along the [001] direction. For the energies of interest, k increases with energy.

For fixed n, equation (1) predicts decreasing QW energies with increasing Cu thickness, which is opposite to the experimental observations in figure 4. Also the oscillation periodicity at the Fermi level from equation (1) is π/k_F instead of the experimental observation of $\pi/|k_{BZ} - \boldsymbol{k}_F|$. It was shown that the oscillation periodicity of magnetic interlayer coupling should be given by $\pi/(k_{BZ} - k_F)$ instead of π/k_F due to the discrete film thickness. For QW states, we can apply a similar idea by taking the Cu thickness as integer multiples (m) of the atomic spacing ($a = 1.8$ Å along [001]); i.e., $d_{\mathrm{Cu}} = ma$. Then equation (1) can by rewritten in terms of a new quantum number ν:

$$2k^e d_{\mathrm{Cu}} - \phi_C - \phi_B = 2\pi\nu \tag{2}$$

where $k^e = k_{BZ} - k, k_{BZ} = \pi/a$ (Brillouin-zone vector), and $\nu = m - n$. Equations (1) and (2) are identical for $d_{\mathrm{Cu}} = ma$, an integral number of layers. Because $k^e = k_{BZ} - k$ decreases with increasing energy, equation (2) now gives an *increase* of the QW energy with increasing d_{Cu} and an oscillation periodicity of $\pi/(k_{BZ} - k_F)$ at the Fermi level, as observed experimentally.

The energies versus thickness for QW states generated by equations (1) and (2) are shown respectively as the red and blue curves in figure 5. The crossing points occur at integer values of m as indicated by the vertical dotted lines. The interesting question to ask then is how the QW states behave between $d_{\mathrm{Cu}} = ma$ and $d_{\mathrm{Cu}} = ma + a$. Will the QW states follow equation (1) or (2)? At noninteger film thickness, the film should consist of atomic steps due to the presence of both $d_{\mathrm{Cu}} = ma$ and $d_{\mathrm{Cu}} = ma + a$. If the terrace length of the steps is very large, the QW states should consists of two sets corresponding to $d_{\mathrm{Cu}} = ma$ and $d_{\mathrm{Cu}} = ma+a$. If the terrace length is small, the QW states will evolve continuously from that of $d_{\mathrm{Cu}} = ma$ to that of $d_{\mathrm{Cu}} = ma + a$. Figure 4 shows that the evolution of the QW states follows equation (2) rather than equation (1).

Is there some physical significance underlying the preference of equation (2)? It is to be noted that the k^e that appears in equation (2) turns out to be characteristic of an envelope function that modulates the QW wavefunction. Some authors [36] have imbued this coincidence with physical significance, and have asserted that the envelope function is somehow essential to the formation of the QW states in the first place. Our finding is that the envelope function is a secondary effect, and we defer discussion of it until section 5. The preference for equation (2) could be due to an energy proximity effect. On increasing the thickness from m to $m + 1$, the new QW state with $n + 1$ half-wavelengths in the well is close in energy to the old state with n half-wavelengths. With the blurring due to imperfect thickness control, the states with constant $m - n$ (rather than constant n) will merge giving rise to apparently continuous curves as shown in figure 4.

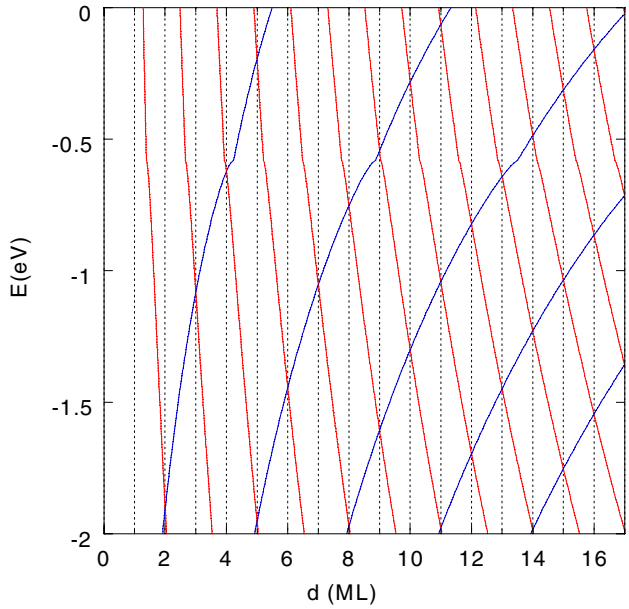

Figure 5. The thickness dependence of the QW energies generated by equation (1) (red curve) is compared with that generated by equation (2) (blue curves). Identical results occur at the crossing points corresponding to integral values of the atomic spacing, *ma* (vertical dotted lines).

The main consideration is the number of half-wavelengths that span the well. For completeness we now discuss how we have treated the end effects embodied in the phase values of ϕ_B and ϕ_C at the Cu/vacuum and Cu/Co interfaces respectively. For the Cu/vacuum interface, an image potential due to electron–hole attraction confines electrons inside the Cu layer. Thus, an electron will propagate an extra distance beyond the physical Cu/vacuum interface until it hits the classical turning point of the image potential. This extra travelling distance plus a phase $-\pi$ due to the reflection by the image potential determines ϕ_B. With the image potential limit being the work function above the Fermi level, it is easy to calculate the Cu/vacuum phase.

$$\phi_B = \pi\sqrt{\frac{3.4\,(\mathrm{eV})}{4.4\,(\mathrm{eV}) - E}} - \pi. \tag{3}$$

Here 4.4 eV is the Cu work function and E is the electron energy measured from the Fermi level. The image potential due to the electron–hole attraction is like a one-dimensional hydrogen atom. That is where the 3.4 eV is from which actually equals one quarter of the hydrogen ionization energy.

For the Cu/Co phase, the *minority-spin* energy band of the Co provides the confinement to the Cu electrons to form the QW states. Thus, the hybridization energy gap of the Co minority-spin band serves as the potential well to the Cu electrons. We choose the convention that the phase evolves from 0 to $-\pi$ from the top to the bottom of the potential well. A convenient *ansatz* for the Cu/Co phase is

$$\phi_C = 2\sin^{-1}\sqrt{\frac{E - E_L}{E_U - E_L}} - \pi. \tag{4}$$

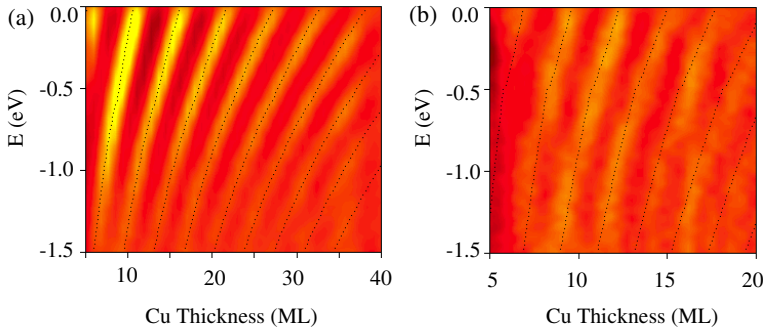

Figure 6. Photoemission intensity along the (a) belly direction, and (b) neck direction of the Cu Fermi surface showing different periodicities with Cu thickness. Dotted curves are calculated results from the PAM.

Here the upper (E_U) and lower (E_L) energies of the potential well are taken from the energy gap of the Co *minority-spin* energy band along [100] ($E_U = -0.58$ eV, $E_L = -3.9$ eV). In this calculation, the Co energy gap was simply treated as a potential energy barrier. This might oversimplify the nature of Co bandgap which comes from the s–d hybridization. Nevertheless, as shown later equation (4) is good enough to describe the QW states in the Cu layer.

To obtain k in equation (1), the Cu sp-conducting electrons are approximated with a nearly-free-electron model which has the following dispersion.

$$E(k) = \frac{\varepsilon_k + \varepsilon_{k-2k_{BZ}}}{2} - \sqrt{\left(\frac{\varepsilon_k - \varepsilon_{k-2k_{BZ}}}{2}\right)^2 + U^2} \qquad \text{with} \quad \varepsilon_k = \frac{\hbar^2 k^2}{2m^*} \tag{5}$$

$2U$ is the energy gap at the BZ boundary, and m^* is the effective mass of the electron. Writing $G = (\hbar^2 k_{BZ}^2/2m)/$, k can be derived as a function of electron energy.

$$\frac{k}{k_{BZ}} = 1 - \left[1 + \frac{E + E_F}{G} - \sqrt{\frac{4(E + E_F)}{G} + \left(\frac{U}{G}\right)^2}\right]^{1/2}. \tag{6}$$

Here the electron energy E is measured from the Fermi level. Equation (6) needs three parameters to be evaluated numerically. We took two parameters from the literature for the Fermi wavevector $k_F = 1.443$ Å^{-1} [37] and the energy at the BZ boundary $E_{X4'} = E(k_{BZ}) - E(k_F) = 1.75$ eV [38]. We could not find a reliable value of the Fermi velocity v_F as the third parameter. Thus we fitted the photoemission data by using the Fermi velocity as a fitting parameter. The fit yields a value of $v_F = 1.15 \times 10^6$ m s^{-1}, which falls in the range between the theoretical value of 1.34×10^6 m s^{-1} [38] and the experimental value of 1.04×10^6 m s^{-1} [39]. The overall agreement in figure 6(a) between the experiment (coloured image) and calculation (dotted curves) demonstrates that the PAM is adequate to describe the QW states in a single-QW system.

To understand the QW energy spectra at the neck of the Fermi surface, k in equation (1) needs to be replaced with the momentum in the normal direction of the film ($k_\perp$). To obtain the Cu/Co phase ϕ_C, the values of upper ($E_U = 0.8$ eV) and lower ($E_L = -0.5$ eV) energies of the Co *minority-spin* energy bandgap at the neck of the Cu Fermi surface should be used [40]. To obtain the Cu/vacuum phase, the parallel component of the wavevector should be taken out of the calculation. The phase ϕ_B can then be calculated from the following formula:

$$\phi_B = \pi \sqrt{\frac{3.4\ (\text{eV})}{4.4\ (\text{eV}) - (E - \hbar^2 k_\parallel^2/2m)}} - \pi. \tag{7}$$

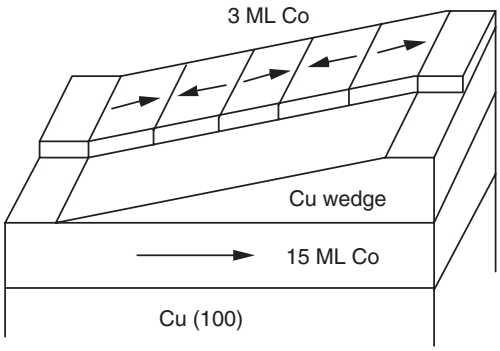

Figure 7. Schematic drawing of the wedge-shaped sample used to obtain the photoemission results of figures 3, 4 and 6. The overlayer of Co was deposited over half the sample and, due to the oscillatory exchange coupling, alternates in magnetization with respect to the Co substrate. The MXLD measurements on this half of the sample can be correlated with the belly and neck periodicities obtained in photoemission from the uncovered half of the sample.

Here $k_{\parallel}$ is the in-plane component of the wavevector which is conserved for ARPES. For the 11° off-normal photoemission at 77 eV, the in-plane momentum is $k_{\parallel} = 0.87$ Å^{-1}. The perpendicular component of the Fermi wavevector ($k_{F\perp}$) was taken as 1.1 Å^{-1}to account for the 2.7 ML oscillation periodicity at the Fermi level. Since the Cu band near the neck of the Fermi surface is very close to the free electron band, we adopted the dispersion of $E(k_{\perp}) = G(k_{\perp}^2/k_{F\perp}^2 - 1)$ with G as the only fitting parameter. The dotted curves in figure 6(b) depict the fitting results using $G = 4.7$ eV. The agreement with the experimental data indicates that the QW states at the neck of the Fermi surface are also accurately described by the PAM.

It is important to point out that E_F at the neck of the Fermi surface is within the Co energy gap ($E_U > E_F > E_L$), in contrast to the belly of the Fermi surface where E_F is above the Co energy gap ($E_F > E_U > E_L$). This difference leads to the formation of the bound QW states at the neck of the Fermi surface as opposed to the resonant QW states at the belly of the Fermi surface [41]. In terms of the PAM, a negative phase ($\phi_C = -0.57\pi$) is derived at the neck of the Fermi surface as opposed to the zero phase ($\phi_C = 0$) at the belly of the Fermi surface. As shown later, this is the origin of the phase relation between the long- and short-period magnetic interlayer couplings.

3.2. Relation between QW states and magnetic interlayer coupling

After understanding the QW states in the Cu layer, we turn our attention to the relation between the QW states and the magnetic interlayer coupling. Because of the short length scale of the oscillation periodicities, a thickness error could have a strong effect on the data analysis. To ensure a direct comparison of the QW states and the magnetic coupling, we covered half of the Cu(wedge)/Co(100) with a 3 ML Co film (figure 7) so that the QW states and the magnetic interlayer coupling are obtained from each half of the sample. In this way, the thickness error between the QW and interlayer coupling measurements is eliminated. For the magnetic coupling measurement, a pulsed magnetic field aligns the magnetization of the 15 ML Co so that the magnetization direction of the top 3 ML Co alternates across the wedged sample according to the sign of the oscillatory magnetic interlayer coupling. Because of the surface sensitivity, the MXLD measures the magnetization of the top 3 ML Co only. Therefore, the MXLD measurements across the Co/Cu(wedge)/Co sandwich identify the sign of the oscillatory interlayer coupling. Images of the DOS at the belly (figure 8(a)) and neck

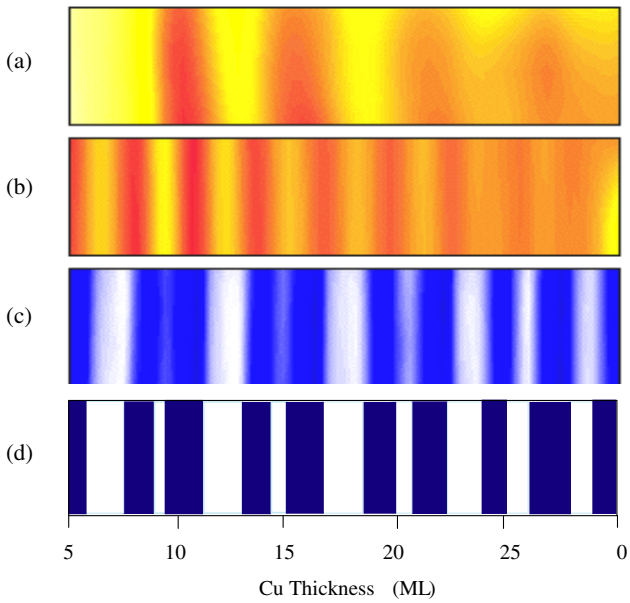

Figure 8. (a) QW states at the belly of the Cu Fermi surface. (b) QW states at the neck of the Cu Fermi surface. (c) XMLD from the top 3 ML Co in figure 7. The dark and light regions correspond to the ferromagnetic and antiferromagnetic interlayer coupling. (d) Calculated interlayer coupling from equation (8).

(figure 8(b)) of the Fermi surface were obtained by scanning the photon beam across the Cu wedge on the Cu/Co(100) side of the sample. Figure 8(c) shows the image of the peak values of the MXLD asymmetry across the Co/Cu/Co(001) side of the sample, with the high- and low-intensity regions corresponding to the AFC and FM couplings, respectively.

The results in figures 8(a) and (b) are equivalent to the optical interference experiment from a wedged glass. From the wedge slope and the separation distance of neighbouring interference fringes, the oscillation periodicities of the QW states at the belly and the neck of the Fermi surface are calculated to be 5.88 and 2.67 ML, respectively. From the MXLD result in figure 8(c), it is easy to see that the magnetic interlayer coupling consists of more than one oscillation periodicity. A Fourier transformation shows that the magnetic interlayer coupling consists of two oscillations with periodicities of exactly 5.88 and 2.67 ML. Therefore we conclude that the long- and short-period oscillations of magnetic interlayer coupling between two Co layers across a Cu spacer layer come from the QW states at the belly and neck of the Cu Fermi surface, respectively. The slight difference between the long periodicity (5.88 ML) and twice the short periodicity (2.67 ML) also results in an interesting beating effect, that increases the width of the short period AFC peaks as Cu thickness increases.

To understand quantitatively the relation between the long- and short-period oscillations, recall that the interlayer coupling is expressed by the formula

$$J = -\frac{A_1}{d_{\mathrm{Cu}}^2}\sin\left(\frac{2\pi d_{\mathrm{Cu}}}{\Lambda_1} + \Phi_1\right) - \frac{A_2}{d_{\mathrm{Cu}}^2}\sin\left(\frac{2\pi d_{\mathrm{Cu}}}{\Lambda_2} + \Phi_2\right). \tag{8}$$

Here d_{Cu} is the Cu thickness, $\Lambda_1 = \pi/k^e_{\perp F1} = 5.88$ ML and $\Lambda_2 = \pi/k^e_{\perp F2} = 2.67$ ML are the long and short periodicities and positive J indicates the AFC. Experimental data are usually fitted with equation (8) to derive the amplitudes and the phases. The relative amplitude A_2/A_1 obviously depends on the interfacial roughness [42]. In fact, earlier studies on the

interlayer coupling showed the existence of long-period oscillations only due to the greater film roughness than the short periodicity. On the other hand, the relative phase is not well understood [42]. Since the magnetic coupling comes from the QW states, the values of Φ_1 and Φ_2 must be intrinsically related to the QW phases at the belly and neck of the Fermi surface. In the QW coupling picture, the Cu electrons see different potential wells for parallel and antiparallel alignment of the two Co layer magnetizations. Thus the coupling is determined by the energy difference of the Cu spacer layer between parallel and antiparallel alignment of the two ferromagnetic layers, i.e. $2J \approx E_P - E_{\mathrm{AP}} = \int_{-\infty}^{E_F} E\,\Delta D\,\mathrm{d}E$, where $\Delta D = D_P - D_{\mathrm{AP}}$ is the difference of the DOS between the parallel and antiparallel alignment of the two ferromagnetic layers. For parallel alignment, the minority bandgap of Co at both sides of Cu forms a QW for the spin down electrons of Cu. As Cu thickness changes, QW state energy levels shift. Whenever a QW state crosses the Fermi level from above, it adds energy to the E_P, making FC unfavourable. Then nature is smart enough to switch the Co magnetization into the antiparallel configuration (AFC) to lower the total energy. When the QW states are truly confined, ΔD is a set of delta functions so that the AFC peak corresponds exactly to the presence of a QW state at the Fermi level. For the resonant states, however, the AFC peak no longer coincides exactly with the QW peak at the Fermi level due to the broadening of the QW state [43, 44]. In the case of Co/Cu/Co(100), the first AFC peak of the long-period oscillations is at ~7 ML [40] which is about a 1 ML shift from the QW peak (~6 ML). Our previous results [28] show that the bulk electron band of Cu works very well for QW states as the Cu thickness is greater than 4 ML. Thus, it is justified to determine the thickness shift from the result of [40]. At the neck of the Fermi surface, the minority spin electrons are completely confined ($E_U > E_F > E_L$, $\Phi_C = -0.57\pi$) so that the quantization condition at the E_F coincides with the maxima of J. Noting that the quantization condition for Co/Cu/Co should be $2k_\perp^e d_{\mathrm{Cu}} - 2\phi_C = 2\pi\nu$ instead of the $2k_\perp^e d_{\mathrm{Cu}} - \phi_C - \phi_B = 2\pi\nu$ for the vacuum/Cu/Co case, it is easy to derive that $\Phi_2 = -\pi/2 - 2\phi_C = 0.64\pi$. At the belly of the Fermi surface, the minority electrons are only partially confined ($E_{\mathrm{L}} < E_U < E_F$, $\Phi_C = 0$) so that the 1 ML shift between the QW peak and the AFC peak has to be taken into account. This will give a phase shift of $2\pi/\Lambda_1 = 0.36\pi$ between the interlayer coupling and the quantization condition at the belly of the Fermi surface, so that $\Phi_1 = \pi/2 - 0.36\pi = -0.86\pi$ With the values of $\Phi_1 = -0.86\pi$ and $\Phi_2 = 0.64\pi$, we used the sign of equation (8) to fit the MXLD result with A_2/A_1 as the fitting parameter. The fitting result, with a value of $A_2/A_1 = 1.2 \pm 0.1$, is shown in figure 8(d) as the white (AFC) and blue (FMC) stripes. The AFC and FMC positions from the fitting agree very well with the experimental data. Since the MXLD measurement gives only the sign of the coupling, we performed a SMOKE measurement to test the amplitude of equation (8). Hysteresis loops were taken from a Co(10 ML)/Cu(wedge)/Co(10 ML) sandwich, and the AFC strength was determined using the same method as in [45]. The result is shown in figure 9 together with the calculated AFC strength from equation (8) using the same A_2/A_1 ratio as in figure 8(d). The overall agreement between the SMOKE results and the calculated AFC strength is very good. The discrepancy in the width of the AF coupling peak is due to the finite size of the SMOKE laser beam. The above results show that the long- and short-period interlayer couplings are well determined by the QW states in k-space.

3.3. Effect of interfacial roughness

One question left is why we omit the effect of film roughness on the phase of QW states. Discrete QW peaks were recently observed in nearly perfect smooth films [46] and demonstrated the accuracy of PAM for a perfectly flat interface. This raises a question: why does the PAM also describe the QW states for films with roughness? Since the PAM describes the quanti-

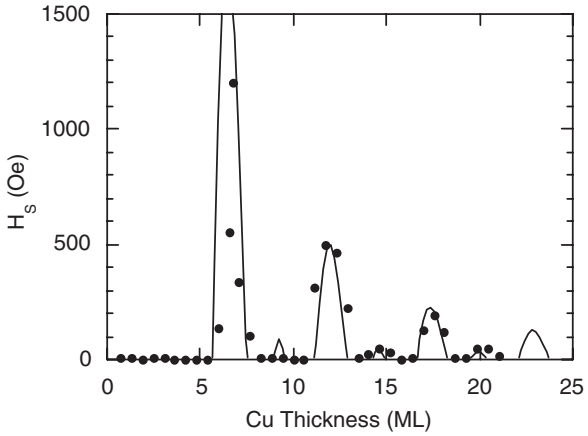

Figure 9. SMOKE measurement across the Co(10 ML)/Cu(wedge)/Co(10 ML) sandwich (solid dots) compared with the calculated results (solid curve) from equation (8) using the same A_2/A_1 ratio as in figure 8(d).

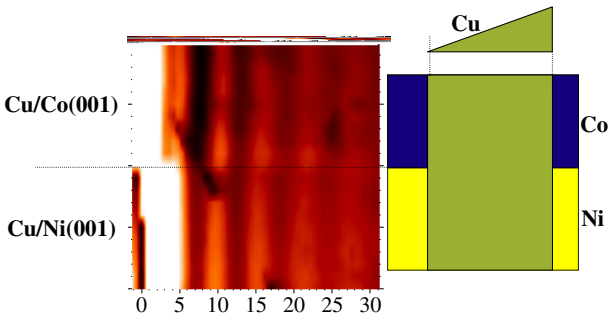

Figure 10. QW states of Cu/Co(001) and Cu/Ni(001) at the belly of the Fermi surface.

zation through phases at the interface, it requires an experimental investigation on whether or not the film roughness affects the phase in PAM. We addressed this question by doing two experiments. In one experiment, we compared the QW states in Cu films grown on Co(100) and Ni(100) which possess different degrees of roughness. In another experiment, we purposely annealed Co/Cu/Co(100) and Co/Cu/Ni(100) sandwiches to introduce interfacial mixing.

We grow the same Cu wedge on Ni and Co in order to have a direct comparison. 7 ML Co film was grown on half of the Cu(001) substrate. The other half was grown by 2 ML Co first and then 7 ML Ni. The 2 ML Co seed layer makes the Ni magnetization in the plane of the film. Then a Cu wedge was grown on top of both Co and Ni (figure 10). As we shall show later, the Cu/Ni interface is rougher than the Cu/Co interface. Photoemission measurements on the Cu wedge were made under normal emission to single out the QW states at the belly of the Fermi surface. To eliminate thickness error due to the misalignment of the Cu wedge relative to the scanning direction, we imaged the QW states in a certain area which covers both Cu/Co(100) and Cu/Ni(100) regions so that the QW peak positions can be compared directly. The results of the photoemission at the Fermi level are shown in figure 10. The oscillations in the image clearly show that the QW states appear at the same Cu thickness for Cu/Co(100) and Cu/Ni(100), i.e. there is no phase shift between these two systems.

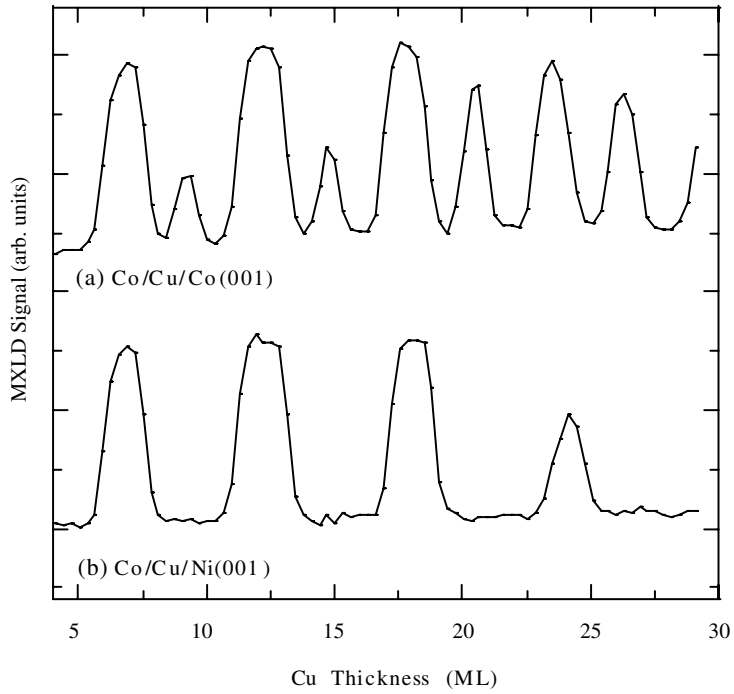

Figure 11. Magnetic coupling measurements on (a) Co/Cu/Co(001) and (b) Co/Cu/Ni(001) systems using MXLD. The absence of the short-period oscillation in Co/Cu/Ni(001) indicates a rougher interface in this system compared with Co/Cu/Co(001). However, the long-period oscillation peaks curve up between these two systems, suggesting that the phase of the QW states does not depend on the interfacial roughness.

After the QW states were measured, a 3 ML Co film was grown on top of the Cu wedge to study the magnetic interlayer coupling. Similar to the previous case, a pulsed magnetic field was applied to align the bottom ferromagnetic layer prior to the measurement. Figure 11 shows the MXLD signal across the Co/Cu/Co(100) and the Co/Cu/Ni(100) sandwiches, with the high- and low-intensity regions corresponding to the AFC and FC, respectively. The Co/Cu/Co(001) exhibits clearly both long- and short-period oscillations in the interlayer coupling. The Co/Cu/Ni(001), however, shows the long-period oscillations only. The absence of the short-period oscillations in Co/Cu/Ni(001) indicates that its interface is rougher than that of the Co/Cu/Co(001). Nevertheless, the long-period coupling peaks appear at the same Cu thickness in both systems, supporting the result of figure 11 that the QW phase at the Fermi level is the same in both systems. Recognizing the different interfacial roughness of these two systems, this result suggests that the film roughness has little effect on the phase of the QW states.

In the second experiment, we progressively annealed the Co/Cu/Co(001) and Co/Cu/Ni(001) samples to promote the interfacial mixing while monitoring the interlayer coupling of the two samples with MXLD. A tungsten filament $\sim$3 mm behind the substrate was used to heat the sample. The annealing temperature was gradually increased by increasing the duration of the annealing time ($\sim$1–4 min) while keeping the filament current at 4 A. Then the sample was cooled to room temperature for the magnetic coupling measurement. Figure 12 shows the MXLD results for both the Co/Cu/Co(001) and Co/Cu/Ni(001) samples after different stages of annealing. Before the annealing, the Co/Cu/Co(001) sample shows both long- and short-period oscillations. After annealing for 3 min ($\sim$200 °C), the short-period

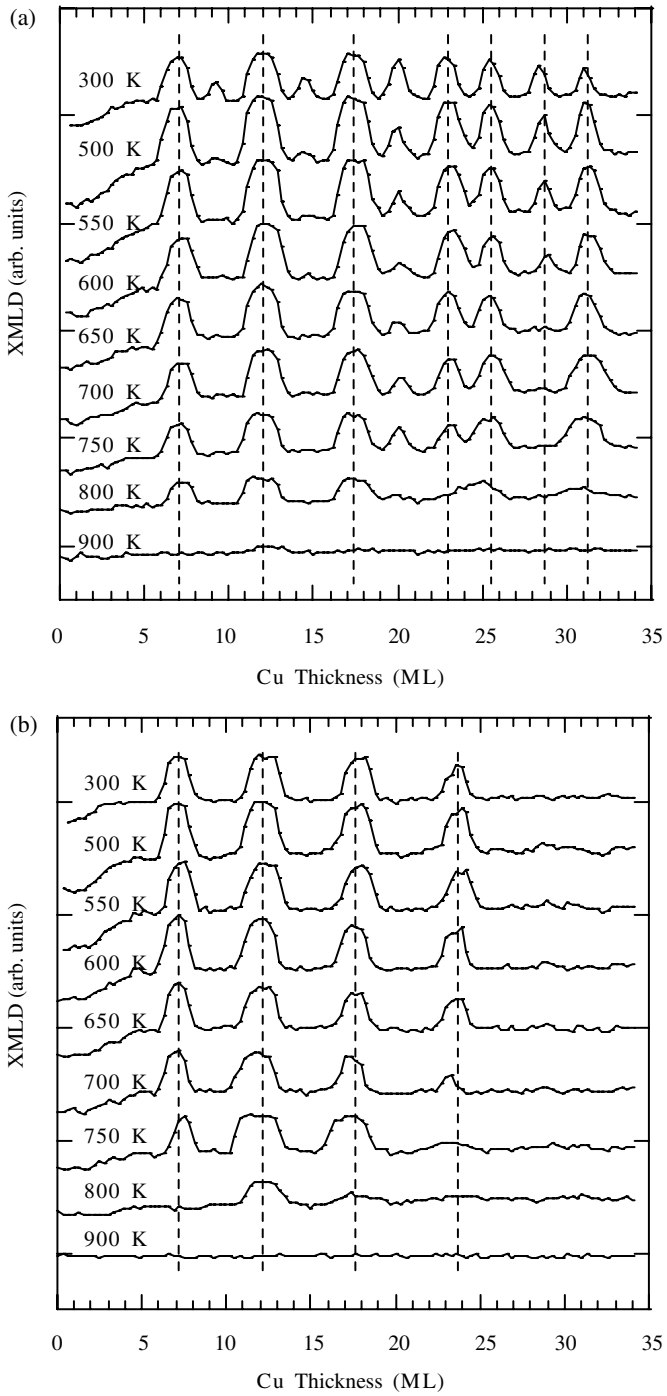

Figure 12. MXLD coupling measurements after annealing at various temperatures for (a) Co/Cu/Co(001) and (b) Co/Cu/Ni(001). While XMLD peaks decrease with increasing annealing temperature, their position as a function of Cu thickness remains unchanged, indicating that the phase of the QW states is not affected by the annealing.

oscillations begin to disappear while the long-period oscillations remain unaffected. After annealing for 4 min (∼300 °C), the short-period oscillations further fade away, especially in the smaller-Cu-thickness regime (0–20 ML) where only the first three peaks of long-period oscillation are present. With further increasing the annealing temperatures, the short-period oscillations gradually disappear even in the thicker part of the Cu wedge. Eventually after 5 min of annealing at 5 A (∼600 °C), even the long-period oscillations vanish. Similar results were also obtained on the Co/Cu/Ni(001) sample. The long-period oscillations begin to be reduced after annealing at 4 A for 10 min (∼400 °C). Eventually, the oscillations disappear after annealing at ∼600 °C. As mentioned earlier, the coupling strength depends sensitively on the interfacial roughness, thus the results in figure 12 show that the annealing indeed promotes the interfacial mixing. On the other hand, the coupling peak positions in both systems remain unchanged after annealing. Noting that the coupling positions are determined by the phase of the QW states, we reach the conclusion that the intermixing or the roughness at the interface does not affect the phase of the QW states.

4. Double quantum wells

So far we have been focusing on single QW states and their relation to the magnetic interlayer coupling. To further develop magnetic nanostructures, it is important to investigate multi-QW systems in which the interaction of electrons from different layers could generate new kinds of electronic state not available in single layers. With this motivation, we carried out an investigation of double-QW systems.

As discussed in the previous section, what we understand so far are (1) quantization and energies are determined by the PAM and (2) the long and short periods of magnetic coupling originate from the belly and neck of the Fermi surface. Although very successful, there are a number of issues that need to be resolved before the next development. For example, it is unclear whether the PAM can be extended beyond a single-QW system. Noting that the quantization specifies which states of bulk materials are allowed in a nanostructure, the key quantity that determines the QW energy levels is the quantum phase Φ. Then the interesting question is: how do QWs from different layers interact each other through the quantum phase Φ at the interface? Obviously, Φ should be determined not only by the energy band mismatching at the interface, but also by the electron wavefunction of a QW state in another layer. This is the issue we address in this section.

4.1. Sample geometry

Our study was greatly facilitated by our ability to prepare *double-wedge* samples as illustrated in figure 13. Two Cu wedges tapered in orthogonal directions are separated by a uniform layer of Ni which serves as the barrier separating two Cu QWs. Structurally, Ni exhibits pseudomorphic growth on Cu(100) so that it should not significantly affect the epitaxial growth of the Cu layer. Electronically, the band structure of Ni is sufficiently different from that of Cu so that it offers an effective barrier to the propagation of electrons between the Cu layers.

By scanning the illuminated spot over the area over the sample, we can find any desired combination of the two QW thicknesses. Along the diagonal AC we have the symmetric case in which the total Cu thickness is varied but the Ni barrier remains at dead centre creating two identical QWs. By scanning parallel to AB or AD, we can keep the thickness of one QW constant while varying the thickness of the other. A third interesting geometry, to be discussed in more detail in section 5, is to scan parallel to the diagonal BD. In this case the total thickness of the Cu remains constant and the Ni layer, if sufficiently thin, may be thought of as a probe that is swept continuously from one face to the other.

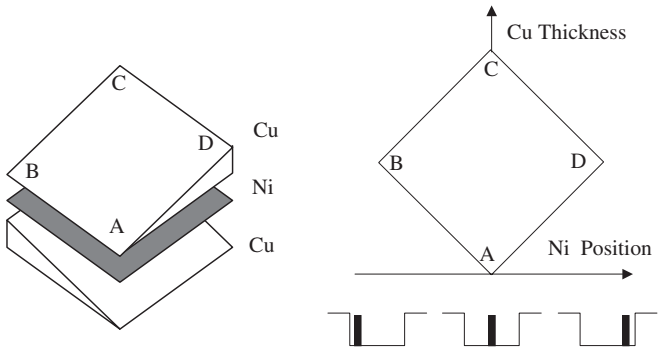

Figure 13. Schematic drawing of the double-wedge sample in which the Cu thickness and the position of the Ni spacer layer can be changed independently. For example, along the diagonal AC, the total thickness of Cu is varied and the Ni barrier remains dead centre. Along the diagonal BD, the total copper thickness is kept constant while the Ni layer is swept from one face to the other.

4.2. Symmetric case

When the Ni barrier is at the centre of the Cu (along line AC in figure 4(a)), it separates the Cu layer into a symmetric double-QW system. Noting that the Ni serves as a potential energy barrier, the propagation of the Cu electron wave across the Ni layer should become more difficult at lower energies. This is associated with a bandgap of bulk Ni (at $\sim$1 eV below the Fermi level) within which free propagation of electrons is prohibited. Thus, we expect the following scenario for two limiting cases based on elementary quantum mechanics. At low energies, the Ni barrier will completely decouple the two Cu QWs to result in degenerate QW states in the two Cu wells. At high energies, the degeneracy of the QW states in the two Cu wells will be lifted by the propagation of the Cu electrons across the Ni barrier, resulting in two nondegenerate QW states with odd and even parities. Figure 14 shows the evolution of the QW states at different energies with 1 ML Ni at the centre of the Cu well (right image). The left image shows the case without the Ni barrier for comparison. At low energies ($|E - E_F| < 1$ eV), we see the degenerate QW states of the separated Cu wells labelled by the quantum number ν'. As the energy increases, we see these states split into pairs. As compared with the case without the Ni barrier, the split pairs evolve into the $\nu = 2\nu' - 1$ and $2\nu'$ states of the Cu well of twice the thickness. Therefore, the result demonstrates that the coupling of the two Cu QWs results in pairs of QW states with odd and even parities.

4.3. Asymmetric case

We then investigated a double QW with one Cu well thickness fixed. To gain a detailed understanding of the double-QW interaction, we measured systematically the energy spectra as a function of the inner Cu thickness (d_{in}) at a fixed outer Cu thickness (d_{out}) as well as energy spectra as a function of the outer Cu thickness at a fixed inner Cu thickness (figures 15(b) and (c)). In this way, we tune the energy levels of one Cu QW by changing the well width while fixing the energy levels of the other Cu QW. Spectra of a single Cu QW on Co(001) are shown in figure 15(a) as a reference. The dashed curves in figure 15(a) are calculated results from PAM [28]. To see the effect of the double-QW interaction, we plot in figures 15(b) and (c) (dashed curves) the locations of QW states that correspond to isolated inner and outer Cu QWs. Recalling that photoemission probes only the outer Cu electronic states, we would expect figures 15(b) and (c) to give results of the isolated outer Cu QW only (dashed curve

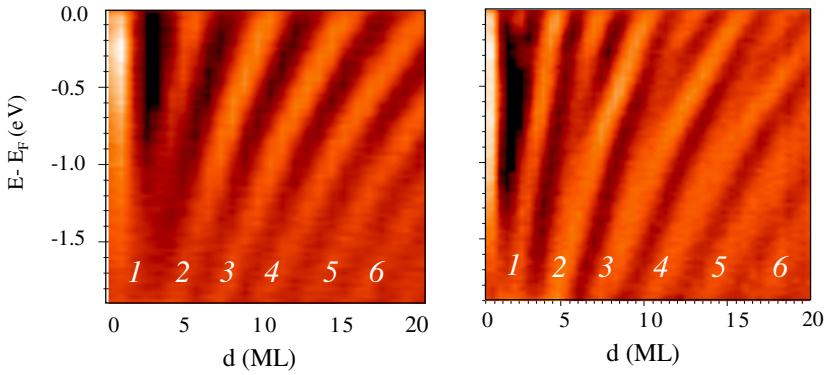

Figure 14. Photoemission spectra for a symmetrical double QW Cu/Ni/Cu (right). As compared with the single-QW states (left), each degenerate QW state of the double QW at low energy splits into two states at high energy with even and odd parities.

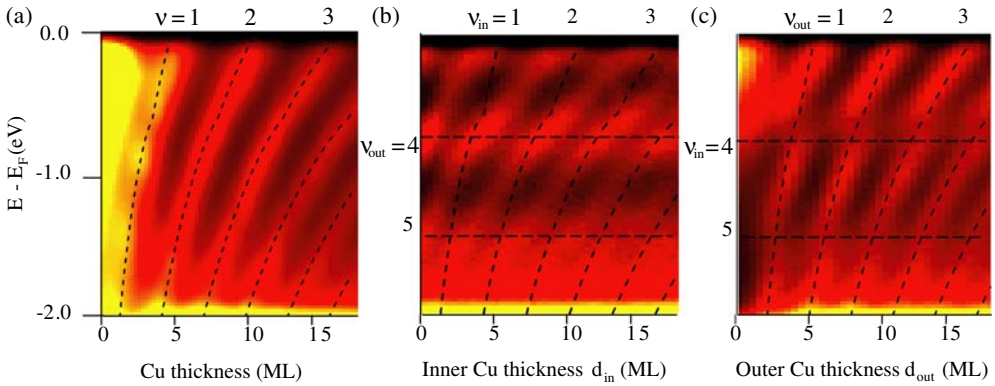

Figure 15. (a) Photoemission spectra in the Cu/Co(001) structure. Dashed curves are calculated results from the PAM for single potential wells. Photoemission intensity as a function of (b) the inner Cu thickness at fixed outer Cu layer thickness of 17 ML and (c) the outer Cu thickness at fixed inner Cu layer thickness of 17 ML. Dashed curves show the binding energies for isolated outer (labelled by quantum number ν_{out}) and inner (ν_{in}) single-QW states, respectively.

labelled by ν_{out}) if the two Cu QWs were totally decoupled. The results distinct from the isolated QW states shown in figures 15(b) and (c) prove electronic coupling between the two Cu QWs. We first discuss the results of figure 15(b). The QW states in this case evolve with the inner Cu thickness in such a way as to avoid the crossing points of states from the two isolated QW states. As the crossing points correspond to degeneracy of the two isolated QWs, the results of figure 15(b) can be easily understood since coupling of two degenerated states would lead to symmetric and anti-symmetric states, which lift the energy degeneracy. As the energy of the ν_{in} state increases for the isolated outer Cu QW, a ν_{in}-like state should first evolve to a ν_{out}-like state once it reaches the same energy level as a ν_{out} state and then evolve back to a ν_{in}-like state as its energy keeps increasing. As a result, a ν_{in} state evolves continuously into a $\nu_{in} + 1$ state as it passes a ν_{out} state. This is exactly what we observed in figure 15(b). Such state crossing between ν_{in}-like and ν_{out}-like states also manifests in the photoemission intensity. As the energy of a ν_{in} state is far from that of a ν_{out} state, the double QW state has mostly the character of the ν_{in} state with the wavefunction residing mainly in the inner Cu

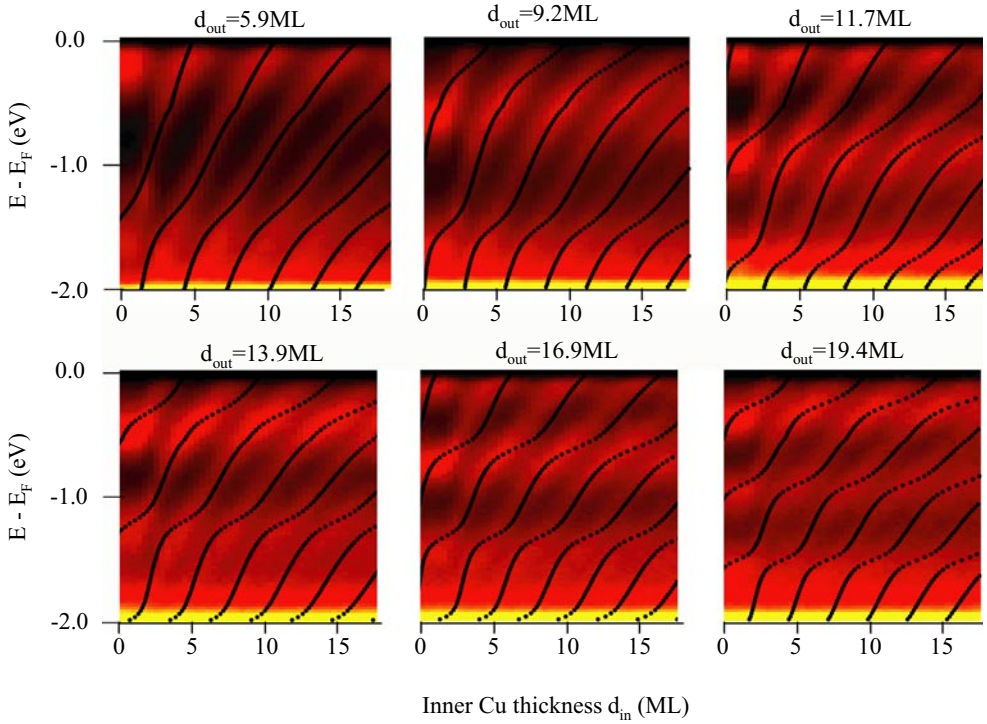

Figure 16. Photoemission intensity as a function of the inner Cu thickness at various fixed outer Cu layer thickness. Dotted curves show the calculated results from the PAM as extended for the double-QW states to include tunnelling through the barrier.

layer, leading to weak photoemission intensity. As the energy of the ν_{in} state evolves with the inner Cu thickness to approach that of a ν_{out} state, the ν_{in} state mixes with the ν_{out} state to acquire the character of the ν_{out} state, leading to high photoemission intensity. As the state passes the ν_{out} state to approach the $\nu_{in} + 1$ state, the electron wavefunction builds up again in the inner layer to giving diminished photoemission intensity. Similar behaviour also occurs in double QWs with fixed inner Cu thickness (figure 15(c)). To confirm that the state crossing occurs in the degeneracy region, we took a series of spectra as a function of inner Cu thickness at various fixed outer Cu thickness as shown in figure 16. It is obvious that state crossing also occurs near the energy levels of the QW states in the fixed Cu layer, supporting our analysis.

4.4. Extension of the phase accumulation model

To do a quantitative analysis, we extended the PAM to calculate the quantization condition of the double-QW states. In PAM, one needs to match the boundary conditions at each interface of the structure. In addition to the Cu/Co phase ϕ_C and the Cu/vacuum phase ϕ_B, additional boundary conditions need to be satisfied at each side of the middle Co barrier. Within the Co, the wavefunction is a superposition of exponentially decayed wavefunctions from the two Cu QWs. For infinitely thick middle Co barrier, there is negligible overlap of the decaying wavefunctions from the two Cu/Co interfaces. This automatically brings us back to the single-QW case. For ultrathin Co barrier, however, the significant overlap of the two decaying wavefunctions inside the Co correlates the boundary conditions at the two Co/Cu interfaces

so that QW states in the two Cu layers have to be adjusted to match the correlated boundary conditions. This is the physical origin of the QW interaction. By introducing a phase ϕ to relate the decaying wavevector κ in the Co barrier to the electron wavevector k in the Cu layer such that $\kappa = -k\tan(\phi/2)$, we found, after some algebra, the quantization condition of the double QWs, given by

$$\tan\left(k^e d_{out} - \frac{\phi_B + \phi}{2}\right) = \frac{\beta \sin\left(k^e d_{in} - (\phi_C - \phi)/2\right)}{\sin\left(k^e d_{in} - (\phi_C + \phi)/2\right) - \beta\cos\left(k^e d_{in} - (\phi_C - \phi)/2\right)} \tag{9}$$

where L is the width of the Co barrier, and β is a barrier tunnelling strength parameter given by

$$\beta = \frac{\sin\phi}{\mathrm{e}^{-2kL\tan(\phi/2)} - 1}. \tag{10}$$

The coupling between the two QWs is embodied in equation (9) through the factor β. Let us consider two limiting cases. For infinitely thick Co, β approaches zero ($-\pi < \phi < 0$ in PAM) so that the solution of equation (9) is $2k^{eff}d_{out} - \phi_{vac} - \phi = 2\pi\nu_{out}$ which is the expected single-QW solution. For L approaching zero, β approaches infinity so that equation (9) yields the solution of $2k^{eff}(d_{out} + d_{in}) - \phi_{vac} - \phi_{\mathrm{Co}} = 2\pi\nu$. This corresponds to the case where the inner and outer Cu layers join together to form a single QW. For $L \sim 1/k$ which corresponds to our experimental condition, equation (9) describes the QW coupling, in particular, the state crossing behaviour. To fit the experimental data, experimental values d_{in} and d_{out}, and bulk Co/Cu value ϕ_C are substituted into equation (9). The calculated results are shown as dashed lines with $L = 1.0 \pm 0.3$ Å. The general trend of the double-QW states, especially the state crossing behaviour, is reproduced reasonably well. Therefore, we conclude that the state crossing comes from the overlap of QW wavefunctions inside the Co barrier.

5. QW wavefunction and its envelope

Up to this point in the article we have considered only QW electron energies and their dependence on QW thicknesses. We now turn to a consideration of the QW wavefunctions and, in particular, their envelope modulation. Experiments with double-wedge samples have indicated that the envelope modulation is actually observable. Our discussion is intended partly as a corrective to assertions that have appeared in the literature [36] that the envelope function is somehow crucial to the existence of the QW states. As we have seen above the systematics of QW formation are determined by the simple quantization condition that an integral number of half-wavelengths should span the well. At no point was it necessary to invoke the existence of an envelope function.

5.1. Particle in a corrugated box

The existence of an envelope function and its physical interpretation can be readily grasped by elaborating the nearly-free-electron (NFE) model [35] for a particle in a corrugated box of the kind illustrated in figure 1(c). We have added to the potential well the lowest Fourier component $U\exp(\mathrm{i}gz)$ with reciprocal lattice vector g corresponding to the periodicity of the lattice ($k_{BZ} = g/2$). Note that the sign of U in figure 1(c) has been chosen to make the atoms 'repulsive', that is to say the maxima are located on the atoms and the minima between the atoms. This choice of sign is necessary to force agreement with first-principles band calculations in the ordering of the p-like and s-like states at the Brillouin zone boundary. In the NFE model we write the wavefunction as

$$\Psi = \alpha_0\exp(\mathrm{i}kz) - \alpha_g\exp[\mathrm{i}(k-g)z]. \tag{11}$$

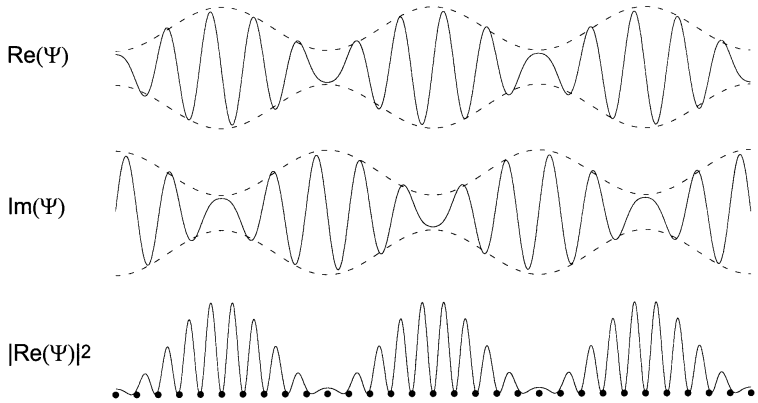

Figure 17. Wavefunctions in a corrugated box. On moving away from the Brillouin zone boundary, the QW wavefunction becomes modulated by an envelope function (dashed curves) characterized by a wavevector $2k^e$ where $k^e = k_{BZ} - k$. The envelope modulation enhances the wavefunction in regions where it is p-like (nodes on the atoms) and depresses it where it is s-like (nodes between atoms) thereby lowering the electron energy.

This is a forward-travelling plane wave of amplitude α_0 interfering with a back-diffracted wave of amplitude α_g. Solving Schrödinger's equation for an infinitely large corrugated box gives the standard NFE result for the $E(k)$ dispersion relation already presented in equation (5). There is the usual NFE gap of magnitude $2U$ at $k = k_{BZ}$. The wavefunctions on either side of the gap are simply $\cos(k_{BZ}z)$ and $\sin(k_{BZ}z)$ which have an oscillating charge density whose periodicity is commensurate with the lattice. For our choice of sign for U, the state of lower energy at the zone boundary will be the so-called 'p-like' state that places its nodes on the atoms and piles its charge density in the potential troughs between the atoms.

As k moves away from k_{BZ}, the periodicity of the charge density becomes incommensurate with the lattice, and the wavefunction acquires an envelope modulation. This is illustrated in figure 17 which shows the real and imaginary parts of Ψ for a representative case. The underlying oscillations are modulated by an envelope function (dashed curves) characterized by a wavevector $2k^e$ where $k^e = k_{BZ} - k$. Note that, contrary to assertions and cartoons published elsewhere, the envelope function should not be treated as a sinusoid of wavevector k^e that multiplies the wavefunction. The physical meaning of the envelope modulation is immediately apparent from the charge density plot shown in the lower part of figure 17. As one traverses the QW, the oscillations in charge density fall progressively in and out of registry with the underlying atomic lattice. The envelope modulation enhances the wavefunction where it is trying to be p-like (nodes on the atoms) and depresses the wavefunction where it is trying to be s-like (charge density on the atoms), consistent with the repulsive sign of U. This is the physical mechanism by which the wavefunction lowers its energy. The envelope modulation is therefore expected on simple physical grounds, but it is a secondary phenomenon that has minimal effect on the quantization condition for the existence of QW states [35].

5.2. Experimental observation of the envelope modulation

With use of wedge-shaped samples it has proved possible to probe the spatial variation of the QW envelope modulation. The method is to perturb the QW states and to measure the response, analogous to the lateral imaging of a metallic surface using scanning tunnelling microscopy (STM), except in our case the tip needs to be replaced with a depth profile probe.

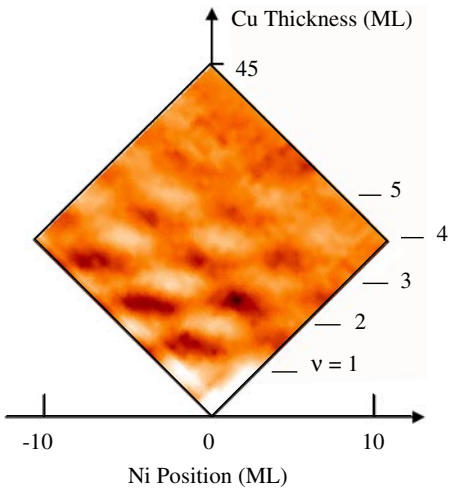

Figure 18. Measured photoemission intensity at the Fermi level for the double-wedge sample depicted in figure 13. Variations in the vertical direction indicate the QW well states labelled by their quantum number ν. Horizontal variations indicate the envelope modulation as the Ni probe layer scans across the well.

Noting that a QW state is an electron standing wave, probing the QW wavefunction is nothing but probing the standing wave of a 'vibrating string'. For a mechanical string, touching the string at antinode or node positions causes considerably different response of the vibration. Thus by systematically changing the contact position along the string, it is easy to map out the spatial variation of the vibration amplitude for a given mode. For the case of the Cu QW state that extends only to a nanometre long, a thin 'finger' is needed to serve as the touching tool. We use 1 ML Ni as a thin 'finger' to touch the nanometre long QW state 'string' at different positions. We chose Ni for both structural and electronic reasons. Therefore, by inserting the Ni layer into different positions of the Cu QW, it should be possible to map out the spatial variation of the envelope function for a given QW state. To systematically vary the Ni position within the Cu QW, we fabricated a double-wedged sample as illustrated in figure 13: two identical Cu wedges were tapered in directions at right angles with 1 ML Ni grown in between. In this double-wedge sample, the Cu thickness and the Ni layer position can be controlled independently. Moving along the diagonal direction BD, the total Cu thickness is constant, but the Ni layer is swept continuously from one side of the Cu QW to the other. Moving along the other diagonal AC has the effect of varying the total Cu thickness while keeping the Ni barrier in the centre. We shall consider both BD and AC variations.

Figure 18 shows the photoemission intensity at the Fermi level across the sample. Two types of oscillation are visible. As a function of Cu thickness (i.e. parallel to AC), we see intensity oscillations with a periodicity of 5.88 ML. This oscillation corresponds to the QW states at the Fermi level within the Cu film (labelled with index ν). Scanning horizontally (i.e. parallel to BD) for each QW state, we also see oscillations as the Ni layer is swept through the Cu film. These oscillations reflect the spatial variation of the Cu QW states as sensed by the Ni layer; i.e., the maximum and minimum intensities correspond respectively to the maximum and minimum positions of the electron standing wave. It is testimony to the usefulness of the wedge-shaped samples that it is possible to determine not only the systematics of the QW energies but also sense the outline of their wavefunctions.

6. Closing remarks

We have presented here a brief review on metallic QW states and their relation to magnetic nanostructures. The examples have been taken from the work of ourselves and colleagues. For a broader review on the context of magnetic nanostructures, the reader is referred to the recent article by Himpsel *et al* [47]. For a more comprehensive survey of metallic QW states, the reader is referred to the recent article by Chiang [48] and the forthcoming article by Woodruff *et al* [49]. We have benefited from numerous interactions and particularly with our collaborators in Berkeley (here follows an alphabetical list): E Arenholz, M O Bowen, H J Choi, T R Cummins, Ernesto J Escorcia-Aparicio, R K Kawakami, W L Ling, S Paik, Eli Rotenberg, J G Tobin, F Toyama, J H Wolfe, Z D Zhang.

Acknowledgments

The work was supported by the US Department of Energy under contract no DE-AC03-76SF00098 at Lawrence Berkeley National Laboratory, and the National Science Foundation under contract no DMR-0110034.

References

[1] Grünberg P, Schreiber R, Pang Y, Brodsky M B and Sowers H 1986 *Phys. Rev. Lett.* **57** 2442
[2] Baibich M N, Broto J M, Fert A, Nguyen Van Dau F, Petroff F, Etienne P, Greuzet G, Friedrich A and Chazelas J 1988 *Phys. Rev. Lett.* **61** 2472
[3] Bennett W R, Schwarzacher W and Egelhoff W F Jr 1990 *Phys. Rev. Lett.* **65** 3169
[4] Brubaker M E, Mattson J E, Sowers C H and Bader S D 1991 *Appl. Phys. Lett.* **58** 2306
[5] Parkin S S P, More N and Roche K P 1990 *Phys. Rev. Lett.* **64** 2304
[6] Pescia D, Kerrkmann D, Schumann F and Gudat W 1990 *Z. Phys.* B **78** 475
Parkin S S P, Bhadra R and Roche K P 1991 *Phys. Rev. Lett.* **66** 2152
[7] Wang Y, Levy P M and Fry J L 1990 *Phys. Rev. Lett.* **65** 2732
Edwards D M, Mathon J, Muniz R B and Phan M S 1991 *Phys. Rev. Lett.* **67** 493
Bruno P and Chappert 1991 *Phys. Rev. Lett.* **67** 1602
[8] Unguris J, Celotta R J and Pierce D T 1991 *Phys. Rev. Lett.* **67** 140
[9] Purcell S T, Folkerts W, Johnson M T, McGee N W E, Jager K, ann de Stegge J, Zeper W B, Hoving W and Grünberg P 1991 *Phys. Rev. Lett.* **67** 903
[10] Purcell S T, Johnson M T, McGee N W E, Coehoorn R and Hoving W 1992 *Phys. Rev.* B **45** 13 064
[11] Fuss A, Demokritov S, Grünberg P and Zinn W 1992 *J. Magn. Magn. Mater.* **103** L221
[12] Qiu Z Q, Pearson J, Berger A and Bader S D 1992 *Phys. Rev. Lett.* **68** 1398
[13] Johnson M T, Purcell S T, McGee N W E, Coehoorn R, ann de Stegge J and Hoving W 1992 *Phys. Rev. Lett.* **68** 2688
[14] Unguris J, Celotta R J and Pierce D T 1992 *1992 March Meeting (Indianapolis, IN)*
[15] Schifgarrde M and Harrison W 1993 *Phys. Rev. Lett.* **71** 3870
[16] Jones B A and Hanna C B 1993 *Phys. Rev. Lett.* **71** 4253
[17] Bruno P 1993 *Europhys. Lett.* **23** 615
[18] Qiu Z Q, Pearson J and Bader S D 1992 *Phys. Rev.* B **46** 8659
[19] Bloemen P J H, Johnson M T, van de Vorst M T H, Coehoorn R, de Vries J J, Jungblut R, aan de Stegge J, Reinders A and de Jonge W J M 1994 *Phys. Rev. Lett.* **72** 764
[20] Okuno S N and Inomata K 1994 *Phys. Rev. Lett.* **72** 1553
[21] Okuno S N and Inomata K 1995 *Phys. Rev.* B **51** 6139
[22] de Vries J J, Schudelaro A A P, Jungblut R, Bloemen B J H, Reinders A, Kohlhepp J, Coehoorn R and de Jonge W J M 1995 *Phys. Rev. Lett.* **75** 4306
[23] Stiles M D 1993 *Phys. Rev.* B **48** 7238
[24] Bruno P 1995 *Phys. Rev.* B **52** 411
Bruno P 1999 *J. Phys.: Condens. Matter* **11** 9403
[25] Miller T, Samsavar A, Franklin G E and Chiang T-C 1988 *Phys. Rev. Lett.* **61** 1404

[26] Ortega J E and Himpsel F L 1992 *Phys. Rev. Lett.* **69** 844
[27] Garrison K, Chang Y and Johnson P D 1993 *Phys. Rev. Lett.* **71** 2801
Carbone C *et al* 1993 *Phys. Rev. Lett.* **71** 2805
[28] Kawakmi R K *et al* 1998 *Phys. Rev. Lett.* **80** 1754
[29] Unguris J, Celotta R J and Pierce D T 1997 *Phys. Rev. Lett.* **79** 2734
[30] Segovia P, Michel E G and Ortega J E 1996 *Phys. Rev. Lett.* **77** 3455
[31] Kläsges R, Schmitz D, Carbone C, Eberhardt W, Lang P, Zeller R and Dederichs P H 1998 *Phys. Rev.* B **57** R696
[32] Curti F G, Danese A and Bartynski R A 1998 *Phys. Rev. Lett.* **80** 2213
[33] Dongqi Li, Pearson J, Bader S D, Vescovo E, Huang D-J and Johnson P D and Heinrich B 1997 *Phys. Rev. Lett.* **78** 1154
[34] Roth Ch, Hillebrecht F U, Rose H B and Kisker E 1993 *Phys. Rev. Lett.* **70** 3479
[35] Smith N V, Brookes N B, Chang Y and Johnson P D 1994 *Phys. Rev.* B **49** 332
[36] Ortega J, Himpsel F J, Mankey G J and Willis R F 1993 *Phys. Rev.* B **47** 1540
[37] Coleridge P T and Templeton I M 1982 *Phys. Rev.* B **25** 7818
[38] Papaconstantopoulos D A 1986 *Handbook of the Band Structure of Elemental Solids* (New York: Plenum)
[39] Halse M R 1969 *Phil. Trans. R. Soc.* **265** 507
[40] Mathon J, Villeret M, Muniz R B, d'Albuquerque e Castro J and Edwards D M 1995 *Phys. Rev. Lett.* **74** 3696
[41] Munoz M C and Perez-Diaz J L 1994 *Phys. Rev. Lett.* **72** 2482
[42] Weber W, Allenspach R and Bischof A 1995 *Europhys. Lett.* **31** 491
[43] Bruno P and Chappert C 1991 *Phys. Rev. Lett.* **67** 1602
[44] Bruno P 1995 *Phys. Rev.* B **52** 411
[45] Qiu Z Q, Pearson J and Bader S D 1992 *Phys. Rev.* B **46** 8659
[46] Paggel J J, Miller T and Chiang T-C 1999 *Science* **283** 1709
[47] Himpsel F J, Ortega J, Mankey G J and Willis R F 1998 *Adv. Phys.* **47** 511
[48] Chiang T C 2000 *Surf. Sci. Rep.* **39** 183–235
[49] Woodruff D P 2002 *Rep. Prog. Phys.* **65** 99